International Journal of Technology (2017) 5: 887-897
ISSN 2086-9614

ABSORPTION CHARACTERISTICS OF THE ELECTROMAGNETIC WAVE AND MAGNETIC PROPERTIES OF THE $La_{0.8}Ba_{0.2}Fe_xMn_{½(1-x)}Ti_{½(1-x)}O_3$ (x = 0.1–0.8) PEROVSKITE SYSTEM

Wisnu Ari Adi[1*], Azwar Manaf[2], Ridwan[3]

[1]*Centre for Science and Technology of Advanced Materials, National Nuclear Energy Agency, Kawasan Puspiptek Serpong, Tangerang Selatan 15310, Banten, Indonesia*
[2]*Department of Physics, Faculty of Mathematics and Natural Sciences, Universitas Indonesia, Kampus UI Salemba, Salemba Raya 4, Jakarta 10430, Indonesia*
[3]*Centre for Technology of Nuclear Fuel, National Nuclear Energy Agency, Kawasan Puspiptek Serpong, Tangerang Selatan 15310, Banten, Indonesia*

(Received: February 2017 / Revised: September 2017 / Accepted: October 2017)

ABSTRACT

This paper reports on the magnetic properties and electromagnetic characterization of $La_{0.8}Ba_{0.2}Fe_xMn_{½(1-x)}Ti_{½(1-x)}O_3$ (x = 0.1–0.8). The $La_{0.8}Ba_{0.2}Fe_xMn_{½(1-x)}Ti_{½(1-x)}O_3$ (x = 0.1–0.8) materials were prepared using a mechanical alloying method. All the materials were made of analytical grade precursors of $BaCO_3$, Fe_2O_3, $MnCO_3$, TiO_2, and La_2O_3, which were blended and mechanically milled in a planetary ball mill for 10h. The milled powders were compacted and subsequently sintered at 1000°C for 5h. All the sintered samples showed a fully crystalline structure, as confirmed using an X-ray diffractometer. It is shown that all samples consisted of LaMnO3 based as the major phase with the highest mass fraction up to 99% found in samples with x < 0.3. The mass fraction of main phase in doped samples decreased in samples with x > 0.3. The hysteresis loop derived from magnetic properties measurement confirmed the present of hard magnetic $BaFe_{12}O_{19}$ phase in all $La_{0.8}Ba_{0.2}Fe_xMn_{½(1-x)}Ti_{½(1-x)}O_3$ (x = 0.1–0.8) samples. The results of the electromagnetic wave absorption indicated that there were three absorption peaks of ~9 dB, ~8 dB, and ~23.5 dB, respectively, at respective frequencies of 9.9 GHz, 12.0 GHz, and 14.1 GHz. After calculations of reflection loss formula, the electromagnetic wave absorption was found to reach 95% at the highest peak frequency of 14.1 GHz with a sample thickness of around 1.5 mm. Thus, this study successfully synthesized a single phase of $La_{0.8}Ba_{0.2}Fe_xMn_{½(1-x)}Ti_{½(1-x)}O_3$ (x = 0.1–0.8) for the electromagnetic waves absorber material application.

Keywords: Absorber; Electromagnetic wave; Lanthanum manganite; Magnetic; Perovskite; Substitution; Structural

1. INTRODUCTION

Most electronic devices that work at high frequency, such as wireless telecommunication systems, local area networks, and other communication equipment, often have noise problems due to electromagnetic wave interference (EMI) (Wu & Li, 2011; Eswaraiah et al., 2011). EMI can reduce the performance of these devices.

Not surprisingly, the demand to eliminate EMI has attracted increased interest as a research

*Corresponding author's email: dwisnuaa@gmail.com, Tel: +62-21-7560-922, Fax: +62-21-7560-926
Permalink/DOI: https://doi.org/10.14716/ijtech.v8i5.871

topic (Eswaraiah et al., 2011). Introducing materials that can absorb electromagnetic waves is an alternative solution to eliminating EMI effects. Some materials, such as radar absorbing materials (RAM) (Mohit et al., 2014), have been reported to exhibit electromagnetic absorption characteristics (Song et al., 2010; Mohit et al., 2014; Sunny et al., 2010) even in the microwave frequency range. To be used in this capacity, electromagnetic wave absorbers must possess the following intrinsic characteristics: permeability (magnetic loss properties) and permittivity (dielectric loss properties). Other characteristics, such as microstructure, thickness, and surface morphology, also determine the absorbing performance of absorber materials. Some studies have reported on absorbers based on doped ferrite magnetic materials (Adi & Manaf, 2012; Duggal & Aul, 2014; Kiani et al., 2014). Likewise, absorbers based on doped dielectric properties have also been found to have absorbing characteristics (Mohit et al., 2014), and tuneable electromagnetic wave absorbers based on combined magnetic and dielectric properties through a composite structure have also been developed (Sunny et al., 2010).

Manganite-based perovskite is another electromagnetic wave absorbing material that has been also developed (Zhang & Cao, 2012; Zhou et al., 2009; Cheng et al., 2010). Manganite-based perovskite is one of the potential candidate materials for microwave absorber applications due to its high permittivity and permeability. Zhang & Cao (2012) succeeded in synthesizing transition metal (TM)-doped $La_{0.7}Sr_{0.3}Mn_{1-x}TM_xO_{3\pm\delta}$ (TM: Fe, Co, or Ni) for microwave absorbing materials. $La_{0.7}Sr_{0.3}Mn_{0.8}Fe_{0.2}O_{3\pm\delta}$ has shown good properties for microwave absorption. The maximum reflection loss was 27.67 dB at a 10.97 GHz frequency, which was obtained from a sample thickness of 2mm. The absorption bandwidth was above 6 dB at a frequency 6.80 GHz (Zhang & Cao, 2012). Additionally, Zhou et al. (2009) reported the successful synthesis of a modified of manganite-based compound. The Mn substituted lanthanum manganite compound composed of $La_{0.8}Sr_{0.2}Mn_{1-y}Fe_yO_3$ ($0<y<0.2$) with a nanostructure was shown to have an excellent microwave absorption characteristic. Nano powders composed of $La_{0.8}Sr_{0.2}Mn_{1-y}Fe_yO_3$ ($0<y<0.2$), which were obtained through synthesis using the sol–gel method, showed absorptions in the 2–18 GHz frequency range. Samples of y = 0.12 and y = 0.14 compositions with a sample thickness of 2 mm showed that the absorption bandwidth reached 8.5 GHz above 8 dB and 6.2 GHz above 10 dB; the highest absorption peak reached 34 dB. To a certain extent, a partial substitution of Mn ions to Fe in $La_{0.8}Sr_{0.2}Mn_{1-y}Fe_yO_3$ ($0<y<0.2$) was believed to affect the interaction of Mn^{3+}–O–Mn^{4+}, causing a break point on the electronic channel resulting in the reduction of the number of hopping electrons (Zhou et al., 2009).

An $LaMnO_3$ system has high permittivity, but low permeability (Mondal et al., 2006). In a previous report (Sardjono & Adi, 2014), barium substituted $La_{0.8}Ba_{0.2}MnO_3$was shown to have ferromagnetic behavior in which the permeability of the material increased. However, the increase in the absorption bandwidth was still relatively low; it only ranged from ~6.5 dB to ~3 dB at a frequency of 14.2 GHz. In this paper, we report on the results of manganite-based materials with $La_{0.8}Ba_{0.2}Fe_xMn_{½(1-x)}Ti_{½(1-x)}$ O_3 (x = 0.1.–0.8) compositions, which were synthesized using a mechanical alloying process. The presence of Ba, Fe, and Ti in the compound should affect the amount of Mn^{3+}/Mn^{4+} coupling; these significantly contribute to the material's magnetic properties thereby increasing its permeability. Therefore, the present study aimed to investigate the nature of the coupling-order parameters and the magnetic properties that are exhibited by this manganite-based compound. The results and discussion focused on the synthesis and characterization of Mn-Ti-doped lanthanum manganite of the perovskite system. This paper discusses the changes in the parameters of the crystal structure, microstructure, magnetic properties, and microwave characterization of this material.

2. MATERIAL AND METHODS

The $La_{0.8}Ba_{0.2}Fe_xMn_{½(1-x)}Ti_{½(1-x)}O_3$ (x = 0.1–0.8) materials were synthesized by a solid reaction method using a mechanical milling technique. This material consisted of a mixture of La_2O_3, $BaCO_3$, Fe_2O_3, $MnCO_3$, and TiO_2, obtained from Merck, with purity (> 99%). The mixture was milled using a high-energy milling (HEM) SPEX 8000 mixer for 10h. The mixture was compacted into pellet shape using 5000 psi of pressure, and then it was sintered in the furnace at 1000°C in the air for 5h and cooled naturally in the furnace.

The phases were identified using the Rigaku MiniFlex X-ray diffractometer (XRD) with an X-ray tube of CuKα. The radiation wave length (CuKα) was 1.5406 Å. The diffraction angles, ranging from 20° to 80°, were measured using continuous scan mode and a step size of 0.02°. The Rietveld analysis was performed using General Structure Analysis System (GSAS) software. The pseudo-Voigt function was used to describe the diffraction line profiles at refinement of the geometry profile (Idris & Osman, 2013). The surface morphology and elemental identification of the sample were analyzed, respectively, using a scanning electron microscope (SEM) and energy dispersive spectroscopy (EDS) (JED 2300, JEOL). The magnetic properties were measured using a vibrating sample magnetometer (VSM) (VSM1.2H, Oxford). The reflection and transmission of the electromagnetic waves were measured using a vector network analyzer (VNA) (R3770, Advantest) with a frequency range specification of 300 kHz–20 GHz. However, the analysis of the reflection and transmission testing result was only performed at a frequency ranging from9 GHz to 15 GHz with a sample diameter of 25 mm and a thickness of 1.5 mm.

3. RESULTS AND DISCUSSION

The phase identification results for the $La_{0.8}Ba_{0.2}Fe_xMn_{½(1-x)}Ti_{½(1-x)}O_3$ (x = 0.1–0.8) samples, measured using XRD, are shown in Figure 1.

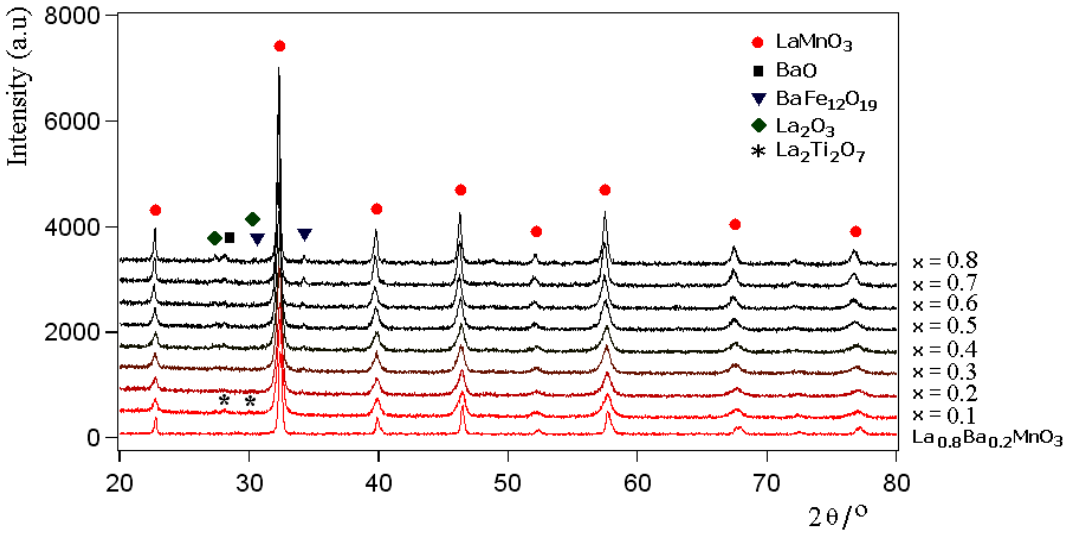

Figure 1 XRD patterns of the$La_{0.8}Ba_{0.2}Fe_xMn_{½(1-x)}Ti_{½(1-x)}O_3$ (x = 0.1–0.8) samples

The qualitative analysis of the XRD patterns refers to the crystallography open database (COD) with card numbers (COD: 1001820), (COD: 2002196), (COD: 1008841), and (COD: 5910030), respectively, for the phases of $LaMnO_3$, $La_2Ti_2O_7$, $BaFe_{12}O_{19}$, and BaO (Figure 1). As seen, the sample with the doping concentration compositions of x = 0.2 and x = 0.3 formed peaks that are believed to be a single phase of $LaMnO_3$. However, some foreign peaks were observed in the samples with the doping concentration compositions of x < 0.2 and x > 0.3, which means that

the samples contain multi-phases. The composition of the x < 0.2 doping concentrationsample consisted of two phases: $LaMnO_3$ and $La_2Ti_2O_7$. The composition of the x > 0.3 doping concentration sample consisted of three phases: $LaMnO_3$, $BaFe_{12}O_{19}$, and BaO.

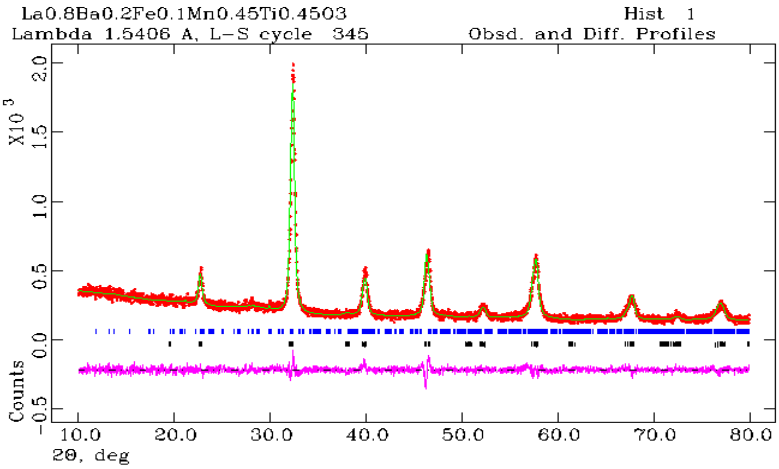

(a) x = 0.1

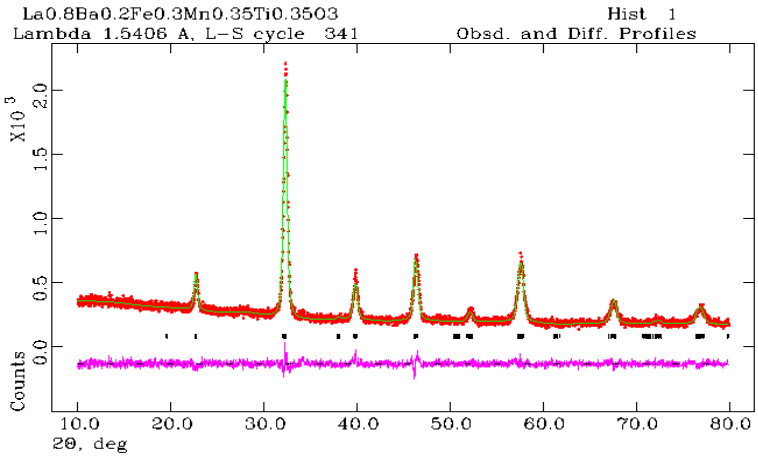

(b) x = 0.3

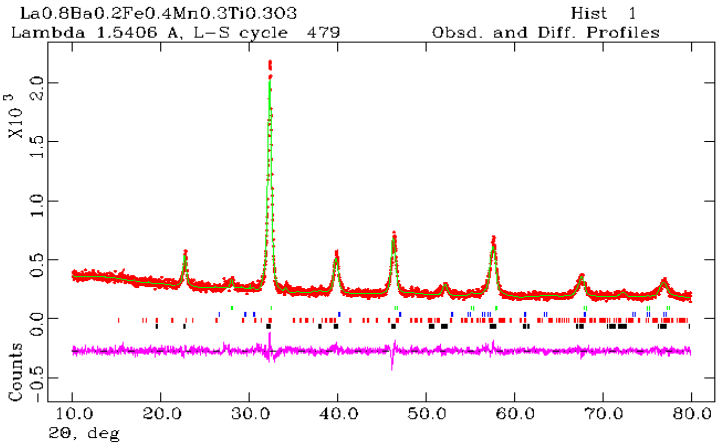

(c) x = 0.4

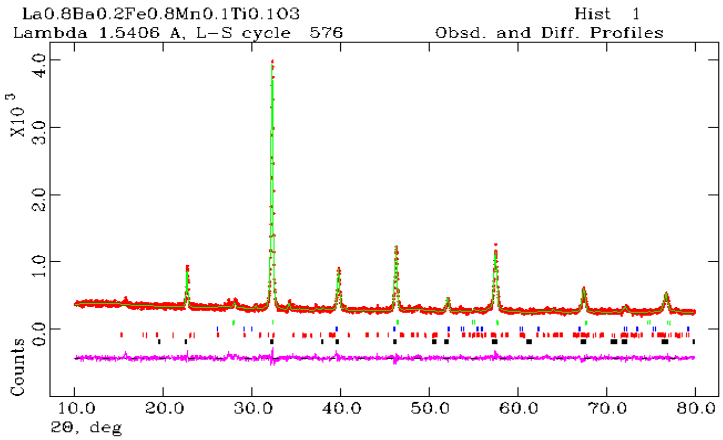

(d) x = 0.8

Figure 2 XRD pattern refinement results for the $La_{0.8}Ba_{0.2}Fe_xMn_{½(1-x)}Ti_{½(1-x)}O_3$ (x = 0.1, 0.3, 0.4, and 0.8) samples

The calculation resulting from the Goldschmidt's tolerance factor showed that the maximum doping concentration of the Ti and Fe substituted into the Mn atom are only around x~0.4 and x~0.3, respectively. Thus, the rest of the components can alter the crystal structure of the material. The crystal structure analysis conducted using GSAS software was required to determine changes in the crystal structure parameters, the amount of mass fraction formed, and the cationic distribution resulting from the substitution of Fe and Ti into the Mn atom, as shown in Figure 2. Figure 2 shows the refinement X-ray diffraction (XRD) pattern on the samples of $La_{0.8}Ba_{0.2}Fe_xMn_{½(1-x)}Ti_{½(1-x)}O_3$ (x = 0.1, 0.3, 0.4, and 0.8).

The XRD pattern refinement results for the $La_{0.8}Ba_{0.2}Fe_xMn_{½(1-x)}Ti_{½(1-x)}O_3$ (x = 0.1–0.8) samples have a very good quality and meet the criteria of fit R_{wp} (R_{wp}< 10%) and the goodness of fit χ^2 (chi-squared of $1 < \chi^2 < 1.3$) (Idris & Osman, 2013). Analysis of the crystal structure was only conducted on the sample with the x = 0.1 doping composition, which represents x < 0.2 and x = 0.3, and the samples with the x = 0.4 and x = 0.8 compositions, which represents x > 0.3. The analysis results for the other compositions are summarized in detail in Table 1.

Results in Table 1 show that $La_{0.8}Ba_{0.2}Fe_xMn_{½(1-x)}Ti_{½(1-x)}O_3$ (x = 0.1–0.8) samples with $La_{0.8}Ba_{0.2}MnO_3$; x=0.2 or $La_{0.8}Ba_{0.2}Fe_{0.2}Mn_{0.4}Ti_{0.4}O_3$ and x=0.3 or $La_{0.8}Ba_{0.2}Fe_{0.3}Mn_{0.35}Ti_{0.35}O_3$ are a single phase materials. A single phase sample with $La_{0.8}Ba_{0.2}Fe_{0.2}Mn_{0.4}Ti_{0.4}O_3$ composition was also previously reported (Manaf & Adi, 2014). Hence, Mn ion in $La_{0.8}Ba_{0.2}MnO_3$ has been successfully substituted partially by Fe and Ti ions. However, it is noted that sample with x > 0 exhibited the increase in unit cell volume over that of non doped $LaMnO_3$ (239.68 $Å^3$). When x = 0.1 a steep increase in the unit cell volume of doped $LaMnO_3$ phase (243.13 $Å^3$) occured before a continuous decrease along with an increase in x up to 0.8 (240.57 $Å^3$). Based on the analysis of changes in the volume of the unit cell, it appears that expansion of the unit cell volume for the $LaMnO_3$ phase occurred in the doping concentrations ranging from x = 0.1 to x = 0.3. Thus, the Mn atom was succesfully substituted by Fe and Ti. The expansion of the unit cell volume for the $LaMnO_3$ phase looks very large because, for the doping concentration of x = 0.1, the biggest substitution is Ti, which has a radii (r = 2.0 Å) larger than the radii of the Mn atom (r = 1.79 Å). The volume of the unit cell of this $LaMnO_3$ phase gradually decreases with increasing doping concentration, which means the content of Ti decreased and the content of Fe increased. The addition of the doping concentration (x > 0.3) results in an imbalance in the reaction; thus there is an excess of Fe, so Fe prefers to bind to Ba to form barium hexaferrite. Because the composition of these compounds is relatively stable, no change in the unit cell volume is seen for the $BaFe_{12}O_{19}$ phase.

Table 1 Detail summary of the refinement results for the crystal structure parameters of the $La_{0.8}Ba_{0.2}Fe_xMn_{½(1-x)}Ti_{½(1-x)}O_3$ (x = 0.1–0.8)

Sample (x)	Phase	Space Group	Lattice parameters			V (Å^3)	Fraction wt%	R_{wp} (%)	χ^2
			a	*b*	*c*				
0.1	$LaMnO_3$	I12/a1	5.527(1)	5.572(1)	7.8605(1)	243.13(7)	97.39	7.98	1.297
	$La_2Ti_2O_7$	$Pna2_1$	25.76(1)	7.85(1)	5.57(1)	1125.5(1)	2.61		
0.2	$LaMnO_3$	I12/a1	5.5315(9)	5.575(1)	7.8608(1)	243.12(7)	100.00	7.75	1.262
0.3	$LaMnO_3$	I12/a1	5.5386(9)	5.577(1)	7.8465(1)	242.88(7)	100.00	7.33	1.221
0.4	$LaMnO_3$	I12/a1	5.5363(1)	5.5822(1)	7.831(1)	242.57(8)	97.76	7.89	1.288
	$BaFe_{12}O_{19}$	P63/mmc	5.856(5)	5.856(5)	23.15(4)	687.9(1)	1.07		
	La_2O_3	P63/mmc	3.863(2)	3.863(2)	6.052(4)	78.2(1)	1.16		
	BaO	Fm-3m	5.512(5)	5.512(5)	5.512(5)	167.5(4)	< 1		
0.5	$LaMnO_3$	I12/a1	5.5475(8)	5.5833(9)	7.822(1)	241.76(6)	96.53	7.80	1.286
	$BaFe_{12}O_{19}$	P63/mmc	5.861(7)	5.861(7)	23.19(5)	688.9(1)	1.81		
	La_2O_3	P63/mmc	3.859(3)	3.859(3)	6.051(1)	77.8(1)	1.70		
	BaO	Fm-3m	5.516(1)	5.516(1)	5.516(1)	169.1(7)	< 1		
0.6	$LaMnO_3$	I12/a1	5.5586(9)	5.5812(9)	7.816(9)	241.44(5)	96.48	7.83	1.291
	$BaFe_{12}O_{19}$	P63/mmc	5.861(5)	5.861(5)	23.14(5)	688.6(1)	2.49		
	La_2O_3	P63/mmc	3.858(7)	3.858(7)	6.051(8)	78.0(2)	1.95		
	BaO	Fm-3m	5.519(9)	5.519(9)	5.519(9)	168.8(1)	< 1		
0.7	$LaMnO_3$	I12/a1	5.5580(7)	5.5917(7)	7.810(6)	240.9(3)	96.07	7.85	1.292
	$BaFe_{12}O_{19}$	P63/mmc	5.855(5)	5.855(5)	23.17(4)	687.1(1)	3.62		
	La_2O_3	P63/mmc	3.856(1)	3.856(1)	6.051(8)	78.1(4)	2.24		
	BaO	Fm-3m	5.523(9)	5.523(9)	5.523(9)	169.0(5)	< 1		
0.8	$LaMnO_3$	I12/a1	5.5580(7)	5.5917(7)	7.810(6)	240.9(3)	96.07	7.91	1.294
	$BaFe_{12}O_{19}$	P63/mmc	5.855(5)	5.855(5)	23.17(4)	687.1(1)	3.62		
	La_2O_3	P63/mmc	3.856(1)	3.856(1)	6.051(8)	78.1(4)	2.24		
	BaO	Fm-3m	5.523(9)	5.523(9)	5.523(9)	169.0(5)	< 1		

Based on the results presented in Table 1, the refinement pattern of the XRD refinement pattern of the $La_{0.8}Ba_{0.2}Fe_xMn_{½(1-x)}Ti_{½(1-x)}O_3$ (x = 0.1–0.8) samples, it is clear that a single phase of the system was found at doping concentrations of x = 0.2 and x = 0.3.

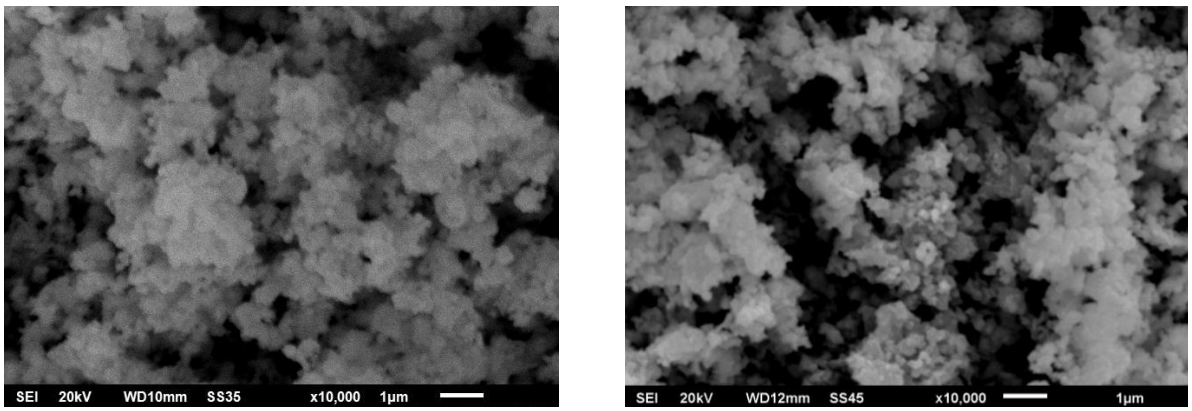

(a) Surface morphology of x = 0.2 (b) Elemental analysis of x = 0.3

Figure 3 SEM photo of the single phase $La_{0.8}Ba_{0.2}Fe_xMn_{½(1-x)}Ti_{½(1-x)}O_3$ (x = 0.2 and x = 0.3) samples

Figures 3a and 3b show the SEM photos of samples x = 0.2 and x = 0.3 respectively showing the surface morphology. While spectrums that resulted from elemental analysis for the two samples were analysed by energy dispersive spectroscopy (EDS) are shown respectively in Figures 4a and 4b. Unfortunately, images of SEM photos are less sharp due to ultra-fine particle morphology. It seems that both samples consisted of nanoparticles with a good homogeneity, uniform across the entire surface.

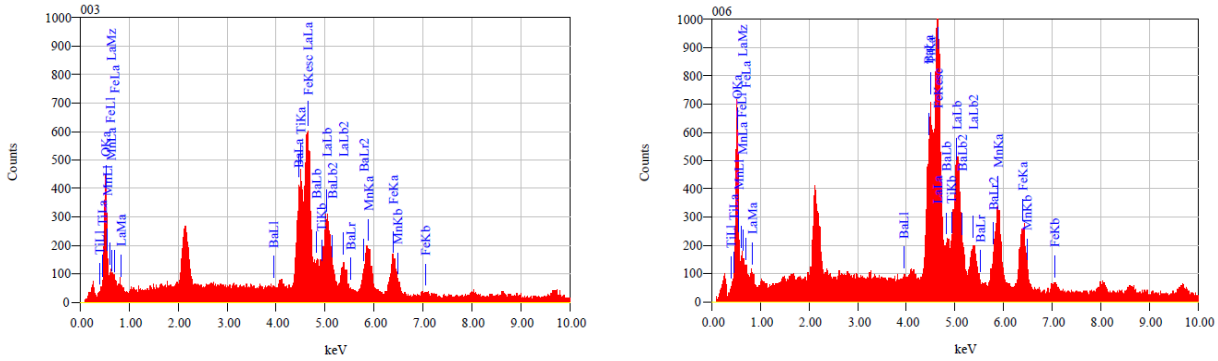

(a) Elemental analysis of x = 0.2 (b) Elemental analysis of x = 0.3

Figure 4 EDS measurement of the $La_{0.8}Ba_{0.2}Fe_xMn_{½(1-x)}Ti_{½(1-x)}O_3$ (x = 0.2 and x = 0.3)

The aggregate particle sizes are estimated around 100 nm. According to the microscopic observation no other minor phases were observed in the two samples. It is again confirmed the result of phase identification by XRD that the two samples are single phase materials. It is also supported by the evidences of elemental analysis results for the two samples as summarized in Table 2.

Table 2 The elementals analysis results by using EDS

No.	Element		Content (at.%), x = 0.2	Content (at.%), x = 0.3
1.	Lanthanum	La	15.90	16.04
2.	Barium	Ba	5.23	4.40
3.	Titanium	Ti	4.43	5.09
4.	Manganese	Mn	6.98	6.30
5.	Iron	Fe	4.33	6.48
6.	Oxygen	O	63.14	61.69

The elemental analysis results show that the phase composition of the x = 0.2 and x = 0.3 samples approach the desired composition. Thus, the single phase of $La_{0.8}Ba_{0.2}Fe_xMn_{½(1-x)}Ti_{½(1-x)}O_3$ (x = 0.2 and x = 0.3) has a very good quality in accordance with the expected stoichiometric composition. Therefore, characterization and further analysis are required to determine the magnetic properties, electric energy, and the electromagnetic wave absorption as a function of the doping concentration of Fe and Ti.

Figure 5 presents the hysteresis loops of the $La_{0.8}Ba_{0.2}Fe_xMn_{½(1-x)}Ti_{½(1-x)}O_3$ (x = 0.1–0.8) samples. It appears that an increase in the doping concentration, x, increases the ferromagnetic properties of the samples.

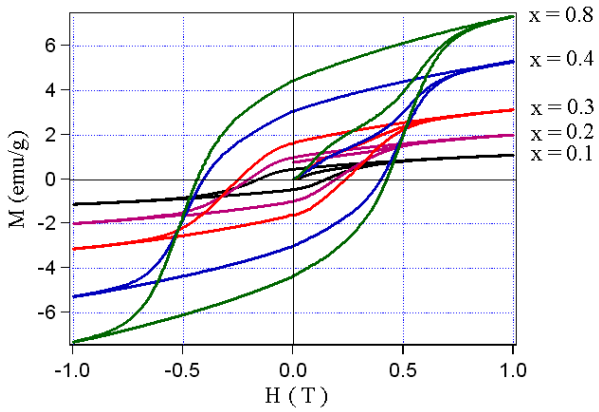

Figure 5 Hysteresis loops ofthe $La_{0.8}Ba_{0.2}Fe_xMn_{½(1-x)}Ti_{½(1-x)}O_3$ (x = 0.1 0.8) samples

All loops show hard magnetic behavior with both remanence and coercivity increased with the doping concentration x. The hard magnetic loop might be rise from $BaFe_{12}O_{19}$ based phase with Ba and Fe ions were partially substituted respectively by La and Mn and/or Ti ions. Hence, the coercivity varies from 0.19 T at x = 0.1 to 0.4 T at x = 0.8. Remanence for all samples increased from 0.44 emu/gr at x =0.1 to 4.31 emu/gr at x = 0.8. Obviously, the remanence value is proportional to the fraction of the hard magnetic phase in the sample. If we refer to the remanence value of 41 emu/gr for a single $BaFe_{12}O_{19}$ phase isotropic magnet, our estimation of the mass fraction of $BaFe_{12}O_{19}$ phase in samples with x = 0.1 and 0.8 are respectively 1.1 % and 10.51 % which are comparable with those calculated from XRD analysis (See Table 1).

Dielectric properties of $La_{0.8}Ba_{0.2}Fe_xMn_{½(1-x)}Ti_{½(1-x)}O_3$ depend on the presence of Mn mixed-valence (Mn ions with different valence) when the La^{3+} cation site is occupied by Ba^{2+} ion, which can be explained in accordance with the theory of double-exchange mechanism. The occurrence of mix-valence the manganese ions in the sample, namely between Mn^{3+} or Mn^{4+} and Fe^{3+} ions, would cause some interactions, which are competing with stoichiometry of $La_{0,8}{}^{3+}Ba_{0,2}{}^{2+}[(Mn_{½\ (x-1)}{}^{3+}Fe_x{}^{3+}Ti_{½\ (x-1)}{}^{4+})_{0,8}(Mn_{½\ (x-1)}{}^{4+}Fe_x{}^{3+}Ti_{½\ (x-1)}{}^{4+})_{0,2}]O_3{}^{2-}$. The amount of Mn^{3+} and Mn^{4+} concentration increases with the presence of Fe^{3+} ions that replace partially the Mn atomic position. Hence, the presence of Fe^{3+} ions as the substituted ion in the sample has generated interaction effects through double exchange and super exchange that occur between ions of Mn^{3+}, Mn^{4+} and Fe^{3+}. The interaction might affects to both magnetic and dielectric properties of sample materials. While the presence of Ti^{4+} ion does not affect the magnetic properties significantly because they have no dipole moment, but its presence can improve its permittivity properties. Figure 6 shows the permeability and permittivity characteristics of the $La_{0.8}Ba_{0.2}Fe_xMn_{½(1-x)}Ti_{½(1-x)}O_3$ (x = 0.1–0.8) samples.

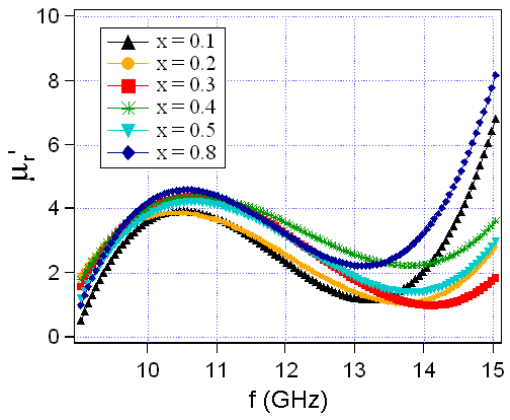

(a) Real permeability

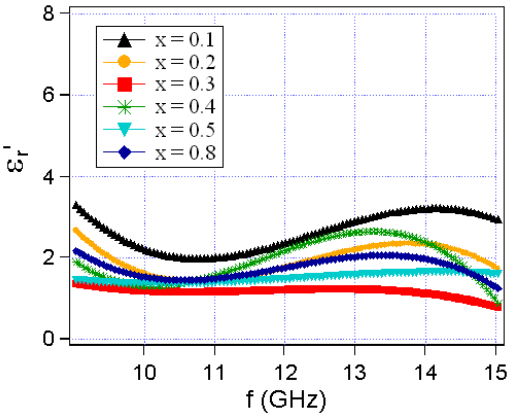

(d) Real permittivity

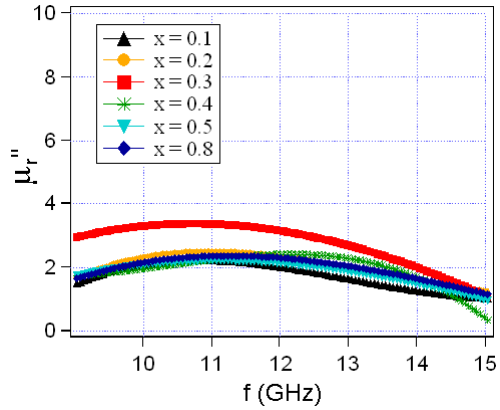

(b) Imaginary permeability

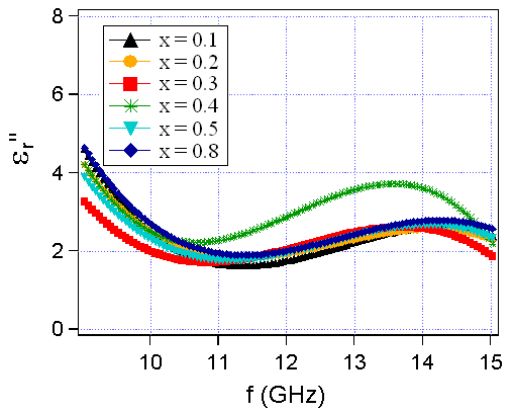

(e) Imaginary permittivity

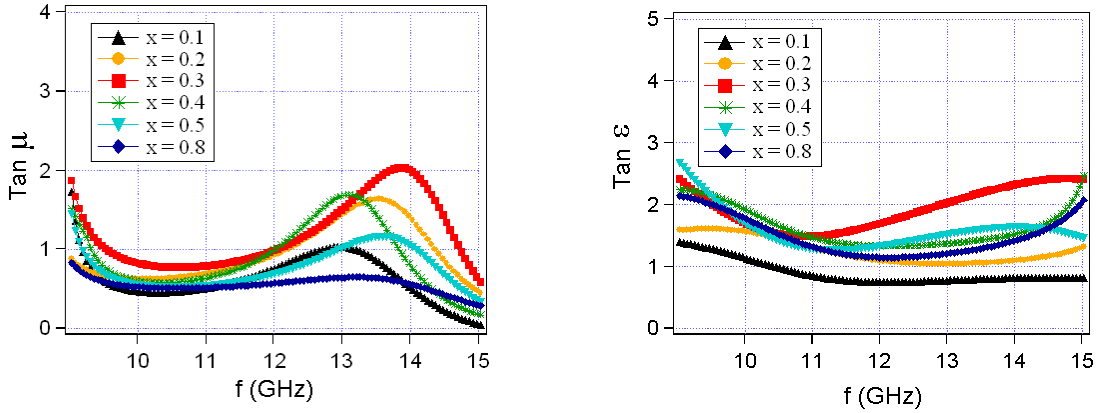

(c) Loss tangent of permeability (f) Loss tangent of permittivity

Figure 6 Permeability and permittivity characteristics oftheof $La_{0.8}Ba_{0.2}Fe_xMn_{½(1-x)}Ti_{½(1-x)}O_3$(x = 0.1–0.8) samples

Figures 6a, 6b, 6d, and 6e show that the complex permeability, $\mu_r = \mu' - j\mu''$, and permittivity, $\varepsilon_r = \varepsilon' - j\varepsilon''$, represent the magnetic and dielectric properties of the electromagnetic wave absorber materials. The real parts, ε' and μ', of the complex permittivity and permeability symbolize the storage capability of the electric and magnetic energy. The imaginary parts ε", μ" represent the loss of electric and magnetic energy. The loss tangent measures the value of the magnetic permeability or electric permittivity that is lost or absorbed in a material. The amount of loss tangent of the permeability and permittivity of this material is shown in Figures 6c and 6f. As an absorber of electromagnetic wave, Fe and Ti, which were partially substituted for Mn on the lanthanum barium manganese oxide, have high imaginary parts in terms of the complexity of the permittivity and permeability, especially in the high frequency range. An increase in the characteristics of the loss tangent μ is caused by the presence of a double exchange interaction between the Mn^{3+}, Mn^{4+}, and Fe^{3+}ions, which contributes to the increase in the ferromagnetic properties of this material. The super exchange interaction between the coupling of the Mn^{3+}, Mn^{4+}, and Fe^{3+}ions contributed to retaining the permittivity of this material.

The reflection loss (RL) measurement results (total absorption) of the $La_{0.8}Ba_{0.2}Fe_xMn_{½(1-x)}Ti_{½(1-x)}O_3$ (x = 0.1–0.8)samples, in the frequency range of 9–15 GHz, are shown in Figure 7. As seen, the $La_{0.8}Ba_{0.2}Fe_xMn_{½(1-x)}Ti_{½(1-x)}O_3$ (x = 0.1–0.8) samples have a relatively significant absorption, and it occurs in a relatively wide range. The electromagnetic wave absorption increased as the doping concentration x increased up to the highest absorption limits on the doping concentration x = 0.3, and then it decreased when the doping concentration was x > 0.3. These results are consistent with the XRD and VSM analyses, which found a single phase for doping concentrations of x = 0.2 and x = 0.3, which have a ferromagnetic behavior of $La_{0.8}Ba_{0.2}Fe_xMn_{½(1-x)}Ti_{½(1-x)}O_3$. The XRD and VSM analyses for the doping concentration of x > 0.3 showed second phases classified as the hard magnetic $BaFe_{12}O_{19}$, which has unfavorable absorption properties. However, for the single phase for the doping concentrations of x = 0.2 and x = 0.3, the highest loss tangent of permeability and permittivity was obtained for the doping concentration of x = 0.3. Thus, in this study the doping concentration x = 0.3 was found to be the optimal composition that can produce a relatively large electromagnetic wave absorption.

Referring to RL plots in Figure 7, it can be seen that that there are three absorption peak frequency with the absorption intensity ~9 dB, ~8 dB, and ~23.5 dB respectively at 9.9 GHz, 12.0 GHz, and 14.1 GHz. The electromagnetic wave absorption reaches 95% at the highest peak frequency 14.1 GHz in the sample of x = 0.3 having sample thickness of relatively thin about 1.5 mm.

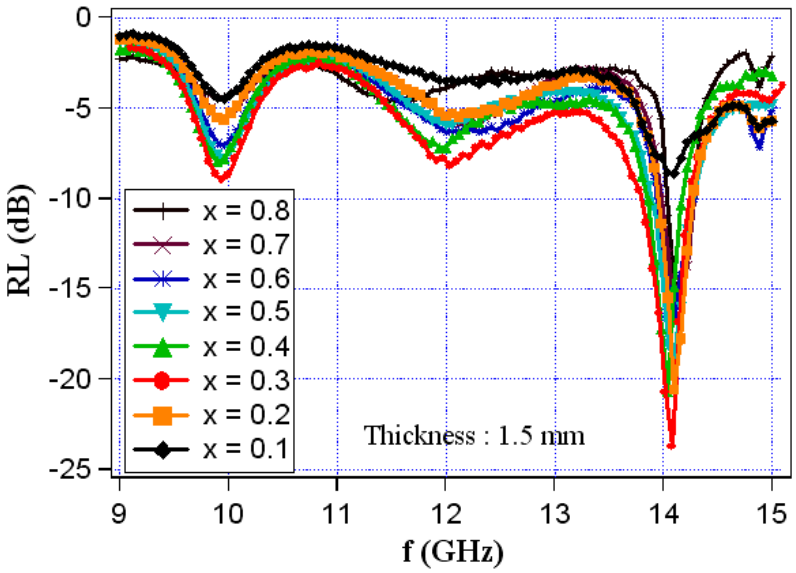

Figure 7 RL curve for the $La_{0.8}Ba_{0.2}Fe_xMn_{½(1-x)}Ti_{½(1-x)}O_3$ (x = 0.1–0.8) samples

The RL value of this sample is comparable with that of the similar type sample, which previously reported (Zhou e al., 2009; Zhang & Cao, 2012). Nevertheless, the results of the current study indicate superior to the previous one where the absorption performance can be similar but the sample thickness of current finding is much less.

4. CONCLUSION

Materials with designated $La_{0.8}Ba_{0.2}Fe_xMn_{½(1-x)}Ti_{½(1-x)}O_3$ (x=0.1–0.8) composition were successfully synthesized through the mechanical alloying process. The $LaMnO_3$ based phase is being the major phase in all samples with the highest mass fraction up to 99 % found in samples with x < 0.3. All samples contained hard magnetic $BaFe_{12}O_{19}$ phase. The microwave absorbing properties of sample with x= 0.3 is the highest among the samples. The electromagnetic wave absorption reaches 95% at the highest peak frequency 14.1 GHz in the sample of x = 0.3 having sample thickness of relatively thin about 1.5 mm.

5. ACKNOWLEDGEMENT

This work wassupported by the Program for Research and Development of smart magnetic material (DIPA 2015), the Center for Science and Technology of Advanced Materials, and the National Nuclear Energy Agency. Many thanks to Dra. Mujamilah, M.Sc. for her kind help in characterizing the use of VSM.

6. REFERENCES

Adi, W.A., Manaf, A., 2012. Structural and Absorption Characteristics of Mn-Ti Substituted Ba-Sr Hexaferrite Synthesized by Mechanical Alloying Route. *Journal of Basic and Applied Scientific Research*, Volume 2(8), pp. 7826–7834

Cheng, Y.L., Dai, J.M., Wu, D.J., Sun, Y.P., 2010. Electromagnetic and Microwave Absorption Properties of Carbonyl Iron/$La_{0.6}Sr_{0.4}MnO_3$Composites. *Journal of Magnetism and Magnetic Materials*, Volume 322, pp. 97–101

Duggal, S., Aul, G.D., 2014. Review on Effect of Electric Permittivity and Magnetic Permeability over Microwave Absorbing Materials at Low Frequencies. *International Journal of Engineering and Advanced Technology*, Volume 3(5), pp. 12–19

Eswaraiah, V., Sankaranarayanan, V., Ramaprabhu, S., 2011. Functionalized Graphene–PVDF Foam Composites for EMI Shielding. *Macromolecular Materials and Engineering*, Volume 296, pp. 1–5

Idris, M.S., Osman, R.A.M., 2013. Structure Refinement Strategy of Li-based Complex Oxides using GSAS-EXPGUI Software Package. *Advanced Materials Research*, Volume 795, pp. 479–482

Kiani, E., Rozatian, A.S.H., Yousefi, M.H., 2014. Structural, Magnetic and Microwave Absorption Properties of $SrFe_{12-2x}(Mn_{0.5}Cd_{0.5}Zr)_xO_{19}$Ferrite. *Journal of Magnetism and Magnetic Materials*, Volume 361, pp. 25–29

Manaf, A., Adi, W.A, 2014. Structural Investigation and Microwave Characteristics of $(Ba_{0.2}La_{0.8})Fe_{0.2}Mn_{0.4}Ti_{0.4}O_3$ Absorbing Materials. *In*: AIP Conference Proceedings 1589, pp. 249–252

Mohit, K., Vibha R.G., Sanjeeb, K.R., 2014. Microwave Dielectric Properties of $Ni_{0.2}Cu_xZn_{0.8-x}Fe_2O_4$ for Application in Antenna. *Progress in Electromagnetics Research B*, Volume 57, pp. 157–175

Mondal, P., Bhattacharya, D., Choudhury, P., 2006. Dielectric Anomaly at the Orbital Order–disorder Transition in LaMnO3+δ. *Journal of Physics: Condensed Matter*, Volume 18(29), pp. 6869–6881

Sardjono, P., Adi, W.A., 2014. Thermal Analysis and Magnetic Properties of Lanthanum Barium Manganite Perovskite. *Journal of Advanced Materials Research*, Volume 896, pp. 381–384

Song, J., Wang, L., Xu, N., Zhang, Q., 2010. Microwave Absorbing Properties of Magnesium-substituted MnZn Ferrites Prepared by Citrate-EDTA Complexing Method. *Journal of Materials Science & Technology*, Volume 26(9), pp. 787–792

Sunny, V., Kurian, P., Mohanan, P., Joy, P.A., Anantharaman, M.R., 2010. A Flexible Microwave Absorber Based on Nickel Ferrite Nanocomposite. *Journal of Alloys and Compounds*, Volume 489, pp. 297–303

Wu, Z., Li, M., 2011. Electromagnetic Interference Shielding of Carbon Nanotube Macrofilms. *Scripta Material*, Volume 64, pp. 809–812

Zhang, S., Cao, Q., 2012. Electromagnetic and Microwave Absorption Performance of Some Transition Metal Doped $La_{0.7}Sr_{0.3}Mn_{1-x}TM_xO_{3\pm1}$ (TM = Fe, Co or Ni). *Materials Science and Engineering B*, Volume 177, pp.678–684

Zhou, K.S., Xia, H., Huang, K.-L., Deng, L.-W., Wang, D., Zhou, Y.-P., Gao, S.-H., 2009. The Microwave Absorption Properties of $La_{0.8}Sr_{0.2}Mn_{1-y}Fe_yO_3$Nanocrystalline Powders in the Frequency Range 2–18 GHz. *Physica B: Condensed Matter*, Volume 404, pp. 175–179